

# Green Chemistry

Cutting-edge research for a greener sustainable future

Accepted Manuscript

This article can be cited before page numbers have been issued, to do this please use: X. Kang, Q. Yang, S. Tang, Z. Chen, S. Budhathoki, R. Paneru, S. Kim, Y. Bai, Q. Li, Z. Chen, A. K. Goroncy, R. N. Zare and M. Fan, *Green Chem.*, 2026, DOI: 10.1039/D5GC04545B.



This is an Accepted Manuscript, which has been through the Royal Society of Chemistry peer review process and has been accepted for publication.

Accepted Manuscripts are published online shortly after acceptance, before technical editing, formatting and proof reading. Using this free service, authors can make their results available to the community, in citable form, before we publish the edited article. We will replace this Accepted Manuscript with the edited and formatted Advance Article as soon as it is available.

You can find more information about Accepted Manuscripts in the [Information for Authors](#).

Please note that technical editing may introduce minor changes to the text and/or graphics, which may alter content. The journal's standard [Terms & Conditions](#) and the [Ethical guidelines](#) still apply. In no event shall the Royal Society of Chemistry be held responsible for any errors or omissions in this Accepted Manuscript or any consequences arising from the use of any information it contains.

## Green Foundation

1. We demonstrate a low-energy, catalyst-free, and renewable feedstock-based strategy to produce high-value nanomaterials, namely carbon quantum dots (CQDs), from agricultural waste (corn stover) using water microdroplets.
2. CQDs of 3–5 nm size with quantum yields up to 20.1% were produced without strong acids or concentrated oxidants. The method avoids liters of 1–10 M HNO<sub>3</sub> or >30% H<sub>2</sub>O<sub>2</sub> solutions typically required in conventional routes.
3. This work can be made greener and elevated by further research on replacing simulated solar light with direct sunlight, further reducing energy demand, on employing recycled or wastewater streams to minimize fresh-water consumption, and by investigating whether residual lignin/cellulose fractions after CQD formation can be valorized, achieving a zero-waste biorefinery model.



## Sustainable Solar-Driven Synthesis of High-Purity Carbon Quantum Dots from Corn Stover for Efficient H<sub>2</sub>O<sub>2</sub> Production from Water

Xuejing Kang<sup>a</sup>, Qian Yang<sup>b</sup>, Sean Xiang Tang<sup>a</sup>, Zhe Chen<sup>a</sup>, Samir Budhathoki<sup>a</sup>, Ramhari Paneru<sup>a</sup>, Soyoung Kim<sup>g</sup>, Yan Bai<sup>c</sup>, Qian Li<sup>c</sup>, Zhongbing Chen<sup>d</sup>, Alexander Goroncy<sup>e</sup>, Richard N. Zare<sup>f\*</sup>, Maohong Fan<sup>g,h\*</sup>

### Abstract

We present a sustainable photocatalytic approach for synthesizing carbon quantum dots (CQDs) from renewable corn stover under simulated solar irradiation. In this process, hydrogen peroxide (H<sub>2</sub>O<sub>2</sub>) is spontaneously and continuously generated at gas-water microdroplet interface. Naturally occurring ferrous (Fe<sup>2+</sup>) and other multivalent ions in the corn stover catalyze the decomposition of H<sub>2</sub>O<sub>2</sub>, producing highly reactive hydroxyl radicals (•OH) that drive the oxidation and fragmentation of lignocellulosic components, ultimately leading to CQD formation. An oxygen-rich environment further facilitates the reaction. Compared to conventional methods, this approach enhances H<sub>2</sub>O<sub>2</sub> utilization efficiency while avoiding excessive oxidation associated with high doses of external oxidants (e.g., H<sub>2</sub>O<sub>2</sub>, HNO<sub>3</sub>). The resulting CQDs (4.6 ± 0.8 nm) exhibit intense blue fluorescence with a quantum yield of up to 20.1 ± 0.8%. Structural analyses (XRD, FTIR, Raman, NMR, XPS) confirm their amorphous graphitic nature with nitrogen self-doping. Uniform CQDs with an average size of 3.1 ± 1.4 nm and high purity were obtained through centrifugation and dialysis purification. This low-cost, scalable method, which integrates *in situ* H<sub>2</sub>O<sub>2</sub> generation

<sup>a</sup> Department of Energy & Petroleum Engineering, University of Wyoming, Laramie, WY 82071, USA

<sup>b</sup> Center for Advanced Scientific Instrumentation, University of Wyoming, Laramie, WY 82071, USA

<sup>c</sup> College of Chemistry and Chemical Engineering, Henan University, Kaifeng, Henan 475004, P.R. China

<sup>d</sup> Department of Applied Ecology, Faculty of Environmental Sciences, Czech University of Life Sciences Prague, Kamýcká 129, 16500 Praha-Suchbát, Czech Republic

<sup>e</sup> Department of Chemistry, University of Wyoming, Laramie, WY 82071, USA

<sup>f</sup> Department of Chemistry, Stanford University, Stanford, CA 94305, USA.

<sup>g</sup> College of Engineering and Physical Sciences, and School of Energy Resources, University of Wyoming, Laramie, WY 82071, USA

<sup>h</sup> College of Engineering, Georgia Institute of Technology, Atlanta, GA 30332, USA

\*Corresponding authors: Richard N. Zare and Maohong Fan

Email: [zare@stanford.edu](mailto:zare@stanford.edu); [mfan@uwyo.edu](mailto:mfan@uwyo.edu).



## Green foundation

1. We demonstrate a low-energy, catalyst-free, and renewable feedstock-based strategy to produce high-value nanomaterials, namely carbon quantum dots (CQDs), from agricultural waste (corn stover) using water microdroplets.
2. CQDs of 3–5 nm size with quantum yields up to 20.1% were produced without strong acids or concentrated oxidants. The method avoids liters of 1–10 M HNO<sub>3</sub> or >30% H<sub>2</sub>O<sub>2</sub> solutions typically required in conventional routes.
3. This work can be made greener and elevated by further research on replacing simulated solar light with direct sunlight, further reducing energy demand, on employing recycled or wastewater streams to minimize fresh-water consumption, and by investigating whether residual lignin/cellulose fractions after CQD formation can be valorized, achieving a zero-waste biorefinery model.

## Keywords

Photocatalytic and efficient synthesis of carbon quantum dots (CQDs), dual-functional corn stover, spontaneous H<sub>2</sub>O-to-H<sub>2</sub>O<sub>2</sub>, Fenton reaction, low-cost and green CQDs

## Introduction

Carbon Quantum Dots (CQDs) are carbon-based nanoparticles, typically less than 10 nm in size, renowned for their exceptional optical, electrical, and chemical properties<sup>1–4</sup>. Since their discovery in 2004<sup>5</sup>, CQDs have received much interest because of their diverse applications in bioimaging, drug delivery, environmental sensing, and clean energy production<sup>6–9</sup>. Their intrinsic photoluminescence, chemical stability, and biocompatibility position them as a promising, nontoxic alternative to traditional semiconductor quantum dots, particularly for sustainable applications<sup>10–13</sup>. Moreover, CQDs offer an eco-friendly nanomaterial solution, potentially reducing costs associated with CO<sub>2</sub> emission control<sup>14–16</sup>.

CQDs have been synthesized through top-down methods, such as laser ablation, arc discharge, and electrochemical exfoliation, which break down larger carbon structures, or bottom-up methods, including chemical oxidation, microwave irradiation, hydrothermal, and pyrolysis techniques, which assemble CQDs from molecular precursors<sup>3,17,18</sup>. Conventional carbon sources include graphite and graphene in top-down approaches, and citric acid or glucose in bottom-up approaches. A promising and sustainable alternative involves synthesizing CQDs from renewable agricultural biomass<sup>19</sup>, promoting a circular economy. However, current biomass-based synthesis methods often rely on concentrated acids, strong oxidants (e.g., H<sub>3</sub>PO<sub>4</sub>, H<sub>2</sub>SO<sub>4</sub>, HNO<sub>3</sub>), and high-temperature reaction conditions, which limit their environmental and economic viability.



Hydrogen peroxide ( $\text{H}_2\text{O}_2$ ) is an environmentally friendly oxidizing agent that decomposes into water, making it attractive for various applications, including bleaching, sterilization, and organic reactions<sup>20</sup>. While some studies have employed Fenton reagents (acidic  $\text{H}_2\text{O}_2/\text{Fe}^{2+}-\text{Fe}^{3+}$ ) or  $\text{H}_2\text{O}_2/\text{W}_{18}\text{O}_{49}$  systems for carbon nanodot synthesis<sup>21–23</sup>, Zare and colleagues demonstrated recently a novel method for *in situ*  $\text{H}_2\text{O}_2$  generation using mechanical energy-driven microdroplets at water-gas and water-solid interfaces<sup>24–28</sup>.

Although microdroplet chemistry has advanced rapidly, prior studies have centered on pure water or simple dissolved molecules, leaving their potential for the green, low-energy conversion of renewable biomass largely unexplored. Here, we report a facile photocatalytic approach for biomass-derived CQD synthesis utilizing the spontaneous  $\text{H}_2\text{O}$ -to- $\text{H}_2\text{O}_2$  conversion strategy. This method operates without external catalysts, strong oxidants, or acids. Specifically, when corn stover is mixed with deionized water and exposed to simulated sunlight,  $\text{H}_2\text{O}_2$  forms *in situ*, enabling the direct synthesis of CQDs. This environmentally benign process provides a mild, scalable, and sustainable route for producing high-quality CQDs from raw lignocellulosic biomass and establishes a foundation for integrating microdroplet reactivity with solar-driven carbon transformation.

## 2. Methods

### 2.1 Materials

The corn stover was purchased from a research field at the University of Wyoming. Quinine sulfate dihydrate, cellulose, hemicellulose (from *Aspergillus*), lignin (alkali-treated), 5,5-dimethyl-1-pyrroline N-oxide (DMPO), quinine sulfate dihydrate ( $\text{C}_{20}\text{H}_{24}\text{N}_2\text{O}_2 \cdot \text{H}_2\text{SO}_4 \cdot 2\text{H}_2\text{O}$ ) and ferrous sulfate heptahydrate ( $\text{FeSO}_4 \cdot 7\text{H}_2\text{O}$ ) were purchased from Sigma-Aldrich.  $\text{O}_2$  (99.999%) and  $\text{N}_2$  (99.999%) were purchased from US Welding Inc. Deionized (DI) water was used throughout this work.

A Power Research Xenon lamp (ozone-free, 1000 W) for simulated solar irradiation was purchased from Newport Corporation (USA). A stander test sieve (Cole-Parmer Essentials Full Height Sieve, No. 18, 1.00mm, USA) was used for particle control. Hydrogen Peroxide  $\text{H}_2\text{O}_2$  Test Strips (low level, 0-100 ppm, Bartovation, USA) were applied to determine the concentration of  $\text{H}_2\text{O}_2$  in aqueous samples. A hotplate magnetic stirrer (Thermo Scientific / IKA C-MAG HS 7, USA) was used to stir and/or heat samples.

### 2.2 Fabrication of corn stover-derived CQDs

The CQDs were synthesized from corn stover (including stalk, leaf, cob, and husk) using an experimental setup under the illumination of Xe lamp. A schematic illustration for the experiment



is shown in the *SI Appendix (Figure S1)*. Dried and cleaned corn stover was used as the sole precursor, which was first ground well by a coffee grinder and then sieved through a 1 mm mesh. Corn stover particles with sizes smaller than 1 mm were collected and used for CQDs preparation. 0.5 g of corn stover powder was mixed with 100 mL of DI water and transferred into a Teflon-lined stainless-steel autoclave equipped with a quartz window. The reactor was placed on a magnetic stirrer plate and stirred the samples vigorously throughout the reaction. A controlled flow rate of pure oxygen gas was introduced into the reactor, and the reaction temperature was continuously recorded. Vacuum filtration with a 0.22  $\mu\text{m}$  membrane filter was employed to remove the unreacted corn stover powder after the reaction. The residue underwent multiple rinses (2–3 times) using DI water during the filtration process. Subsequently, the liquid sample was subjected to evaporation in a VWR 1330FM mechanical oven (Marshall Scientific, USA) maintained at 50°C, while maintaining a final CQD solution volume of 100 mL. The obtained CQD solutions were then stored under refrigeration (4 °C) for subsequent experimental applications.

### 2.3 Characterization of CQDs

The three-dimensional emission-excitation-intensity fluorescence spectrum (3D-EEM) were performed on a spectrofluorometer (Fluorolog-3, Horiba, USA), and the photoluminescence property of CQDs was determined by shifting the excitation wavelengths within 200–600 nm (slits: 4 nm) with an increase of emission wavelengths from 200 to 700 nm (slits: 2 nm). Ultraviolet-visible (UV-vis) absorption spectroscopy was done using a UV-spectrophotometer (Shimadzu).  $^1\text{H}$ -NMR and  $^{13}\text{C}$ -NMR spectra were measured using a Bruker Avance III 600 MHz spectrometer with deuterium oxide ( $\text{D}_2\text{O}$ ) as the solvent. Fourier transform infrared (FTIR) spectrum analysis was performed using a spectrophotometer instrument with non-destructive attenuated total reflectance (ATR) technology (Nicolet iS50, Thermo Scientific, USA). The prepared CQDs were scanned 64 times at a resolution of 16  $\text{cm}^{-1}$ , with a wavenumber range of 4000–400  $\text{cm}^{-1}$ . X-ray diffraction (XRD) analysis was conducted using an X-ray diffractometer (Rigaku, Japan) with a scanning rate of 4°  $\text{min}^{-1}$ , ranging ( $2\theta$ ) from 10° to 90°. The FTIR and XRD were employed to determine the structural characteristics of CQDs. X-ray photoelectron spectroscopy (XPS, Kratos Axis Ultra DLD) was used to determine the surface chemical compositions. ESR spectra were collected on a Bruker EMX EPR spectrometer (X-band,  $\sim 9.87$  GHz) using DMPO as a spin trap, to detect the measurements (*SI Appendix, text S7*).

Morphological characterization was carried out using high-resolution transmission electron microscopy (HR-TEM, JEOL JEM-2100F, Japan) with ultra-thin amorphous film-supported copper grids. The elemental composition of the corn stover was determined using a vario MACRO cube elemental analyzer (Elementar), with the oxygen content estimated by the subtraction method (*SI Appendix, Table S2*). Raman spectra were conducted using a DXR2 Raman spectrometer with



a 532 nm excitation laser in the range of 1000–2000  $\text{cm}^{-1}$  to analyze the structural characteristics of CQDs. The thermal stability of the samples was determined using a simultaneous thermal analyzer (DSC/TGA SDT Q600). Liquid chromatography-mass spectrometry (LC-MS) analysis was performed on an Agilent 1260 infinity HPLC system coupled with a 6120 Quadrupole MS equipped with a Hi-Plex H column. Inductively coupled plasma mass spectrometry (ICP-MS) and ion chromatography (IC) analyses were performed using a Thermo iCAP RQ single quadrupole mass spectrometer and a Thermo ICS 6000 system, respectively. A pH meter (Mettler Toledo SevenCompact S220, Switzerland) was used to measure the pH values of the aqueous CQDs samples.

## 2.4 Quantum yield measurements

The fluorescence quantum yield (QY) is the ratio of fluorescence photons emitted to excitation photons absorbed. The QYs of the prepared CQDs were evaluated by comparing their integrated photoluminescence (PL) intensities under 340 nm excitation. Quinine sulfate dihydrate in 0.1 M  $\text{H}_2\text{SO}_4$ , with a refractive index ( $\eta$ ) of 1.33 and a quantum yield of 0.54 at 350 nm excitation, was used as the standard reference. The CQDs were dissolved in deionized water (refractive index  $\eta = 1.33$ ) and evaluated at a specific concentration, ensuring that their absorbance value remained below 0.1 at 350 nm. The absorbance at the excitation wavelength of 350 nm was measured using a UV-Vis spectrophotometer (Shimadzu). The photoluminescence emission spectra of the solutions were recorded using a fluorescence spectrometer (Fluorolog-3, Horiba, USA) at an excitation wavelength of 350 nm, with both excitation and emission slit widths set to 2 nm. The integrated PL intensity, representing the total emission within the wavelength range of 300–700 nm, was determined as the area under the PL curve. The QY was calculated using the following equation<sup>29</sup>:

$$QY_{CQDs} = QY_{ST} \left( \frac{A_{CQDs}}{A_{ST}} \right) \left( \frac{I_{ST}}{I_{CQDs}} \right) \left( \frac{\eta_{CQDs}^2}{\eta_{ST}^2} \right) \quad (\text{Eq. 1})$$

Here, QY denotes the fluorescence quantum yield, “A” represents the measured integrated fluorescence intensity and absorbance, “I” denotes the absorbance value, and “ $\eta$ ” refers to the refractive index of the solvent. The subscripts “CQDs” and “ST” denote the aqueous CQDs solutions and the standard solution of QS, respectively.

## 3. Results and Discussion

### 3.1 Factors Affecting CQD Synthesis Without External $\text{O}_2$ Introduction

Initial experiments (*SI Appendix, Table S1*) were conducted to evaluate the feasibility of generating hydrogen peroxide ( $\text{H}_2\text{O}_2$ ) from water under solar irradiation without the introduction of external



oxygen (O<sub>2</sub>). As shown in *SI Appendix (Figure S1e)*, H<sub>2</sub>O<sub>2</sub> accumulated to approximately 50–100 ppm under simulated solar light (>260 nm) within five hours, primarily due to the condensation of water vapor<sup>26</sup>.

Fluorescence and UV-vis spectroscopy analyses (*SI Appendix, Figure S2*) revealed that the highest fluorescence intensity was achieved at a light intensity of 834 mW cm<sup>-2</sup>. Further optimization of reaction duration at this light intensity (*SI Appendix, Figure S3*) revealed that 96 h was the optimal duration. The highest-performing sample (*Sample 6*) exhibited emission peaks at excitation wavelengths of 420–470 nm and 320–370 nm, as characterized by its 3D-EEM fluorescence spectrum (*Figure S3d*). The quantum yield of *Sample 6* was evaluated as 13.7% (*SI Appendix, Table S4*).

HRTEM images of *Sample 6* revealed CQDs with an average size of 29.8 ± 13.5 nm (Figures 1a and 1b). Additionally, larger CQDs (50–100 nm) and irregular carbon sheets with graphite-like structures were observed (Figure 1c) in the sample. Under UV irradiation (365 nm), the CQDs exhibited blue-green fluorescence (Figure 1b), despite their size nonuniformity. Their crystal lattice spacing of 0.21 nm was measured, corresponding to the (11̄00) lattice planes of graphitic carbon, in agreement with prior studies<sup>3</sup>. The UV-vis spectrum (*SI Appendix, Figure S3f*) displayed peaks at 232 nm and 278 nm, associated with the π → π\* transition of C=C bonds and the n → π\* transition of carbonyl groups (C=O), respectively, consistent with previously reported CQDs.

The temperature of the aqueous *Sample 6* solution reached ~50 °C under an intensity of 834 mW cm<sup>-2</sup> irradiation (*SI Appendix, Figure S3f*). To distinguish photothermal effects from photocatalytic contributions, a control experiment (*SI Appendix, Table S1, Sample 8*) was conducted by heating the solution to 50 °C for 96 h in the absence of light (*SI Appendix, Figure S1c*). HRTEM image (Figure 1d) revealed that *Sample 8* contained larger CQDs (69.4 ± 20.5 nm) (Figure 1e) without graphite-like structures. Although its UV-vis spectrum (Figure 1f) showed absorption peaks at 232 nm and 280 nm similar to those of *Sample 6*, its 3D-EEM fluorescence spectrum (Figure 1g) exhibited significantly lower fluorescence performance than that of *Sample 6* (*SI Appendix, Figure S3d*). The CQDs from *Sample 8* emitted green fluorescence (Figure 1e), which is attributed to increased particle size heterogeneity. The quantum yield of *Sample 8* was 9.0% (*SI Appendix, Table S4*). These findings suggest that both thermal effects and photocatalytic reactions, particularly H<sub>2</sub>O-to-H<sub>2</sub>O<sub>2</sub> conversion, are crucial for CQD formation and optical enhancement.

To further decouple the effects of illumination and oxygen availability, additional control experiments were conducted under conditions of dark with O<sub>2</sub> (*Samples 18*), and light with N<sub>2</sub> (*Samples 19*), which are described in *Text S6* and *Figure S7*. Through their 3D-EEM results, almost no fluorescence (*Figure S7a*) was observed in *Sample 18*, demonstrating that oxygen alone—



without illumination-driven interfacial activation—is difficult to generate detectable amounts of CQDs. Conversely, illumination in the absence of a continuous oxygen supply (light with N<sub>2</sub>, *Sample 19*) produced CQDs with quite weak fluorescence (*Figure S7b*) due to the O<sub>2</sub>-deficient environment. When considered together with the light with atmosphere environment (*Sample 6*), light with O<sub>2</sub>-rich environment (*Sample 10*), and dark with external heating (*Sample 8*) experiments, these results confirm that both illumination and oxygen are simultaneously required for high efficiency of CQD formation.

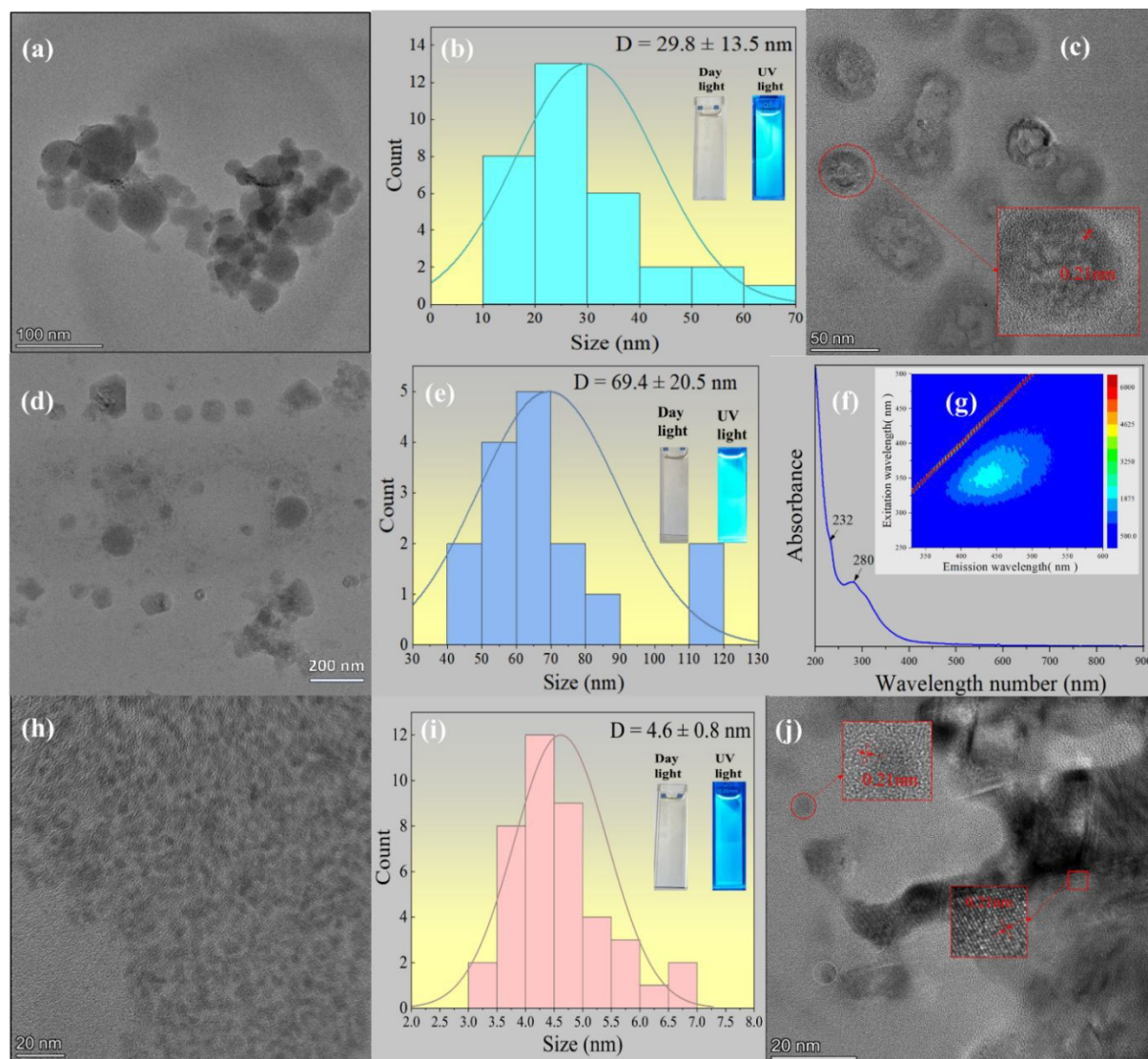


Figure 1 (a-c) Characterization of CQDs (*Sample 6*): (a) HRTEM image with amorphous structure (scale bar: 100 nm), (b) Size distribution of the CQDs and the photograph of CQDs solution under daylight and a handheld UV flashlight (Alonefire SV003, SVC 365 nm), (c) HRTEM image with graphite structure (scale bar: 50 nm); (d-g) Characterization of CQDs (*Sample 8*): (d) TEM image with amorphous structure (scale bar: 200 nm), (e) Size distribution of the CQDs and the photograph



of CQDs solution under daylight and a handheld UV flashlight, (f) UV-vis absorption spectrum, (g) 3D-EEM fluorescence spectrum; (h-i) Characterization of CQDs (*Sample 10*): (h) HRTEM image with amorphous structure (scale bar: 20 nm), (i) Size distribution of the CQDs and the photograph of CQDs solution under daylight and a handheld UV flashlight; (j) HRTEM image with graphite structure including zoomed-in view (scale bar: 20 nm).

### 3.2 Factors Affecting CQD Synthesis with External O<sub>2</sub> Introduction

Additional experiments were conducted with O<sub>2</sub> introduction to synthesize uniform, high-performance CQDs. The effect of O<sub>2</sub> flow rate on CQDs synthesis was investigated (*SI Appendix, Table S1, Sample 9-11*). The results (*SI Appendix, Figure S4*) show that the *Sample 10*, synthesized at an O<sub>2</sub> flow rate of 28 mL min<sup>-1</sup>, exhibited optimal fluorescence performance. HRTEM images of *Sample 10* (Figure 1h and 1i) revealed a monodisperse CQD population with an average diameter of 4.6 ± 0.8 nm. In addition, graphite sheets and some graphite-like quantum dots (5-10 nm) with a lattice spacing of 0.21 nm were observed (Figure 1j), consistent with those observed in *Sample 6* (Figure 1c). Notably, the quantum yield of *Sample 10* reached 20.1 ± 0.8% (*SI Appendix, Table S4*), which is more than double that of *Sample 8* (9.0%) synthesized under dark conditions with external heating at the same temperature.

The structural characterization of CQDs (*Sample 10*) synthesized under O<sub>2</sub>-rich conditions was performed using XRD, ATR-FTIR, Raman spectroscopy, NMR, and XPS. The XRD pattern (Figure 2a) exhibits a broad diffraction peak at 21°, corresponding to the (002) plane of amorphous graphite (JCPDS: 41-1487), indicating low graphitization<sup>30</sup>. ATR-FTIR spectra (Figure 2b) identified characteristic functional groups, including O-H/N-H (3500–3000 cm<sup>-1</sup>), C-H (2930 cm<sup>-1</sup>), C=C (1580 cm<sup>-1</sup>), C-O (1243 cm<sup>-1</sup>), and C=O (1690–1740 cm<sup>-1</sup>)<sup>31-34</sup>. The obtained Raman spectrum (Figure 2c) was baseline-corrected and fitted using Gauss functions, revealing the characteristic D band (~1348 cm<sup>-1</sup>) and G band (~1573 cm<sup>-1</sup>) associated with disordered and graphitic sp<sup>2</sup> carbon, respectively. An I<sub>D</sub>/I<sub>G</sub> ratio of 1.4 calculated based on the integrated peak areas of the fitted bands indicates a high level of structural disorder relative to the graphitic content<sup>35</sup>.

NMR spectroscopy (Figures 2d and 2e) shows proton signals at 1–3 ppm (sp<sup>3</sup> C-H), 3–6 ppm (oxygenated groups), and 8–10 ppm (aldehydic protons). The <sup>13</sup>C NMR spectrum displays signals at 20–80 ppm (sp<sup>3</sup> carbon), 80–100 ppm (ether-bound carbon), 100–120 ppm (aromatic carbon), and 170–185 ppm (carboxyl or ester C=O)<sup>36,37</sup>. XPS analysis (Figures 2f–i) indicates peaks corresponding to C-C/C=C, C-O/C-N, and C=O in the C-1s spectrum, while O-1s/N-1s spectra confirmed the presence of oxygen-containing functionalities and pyridinic-N/amide-N species.



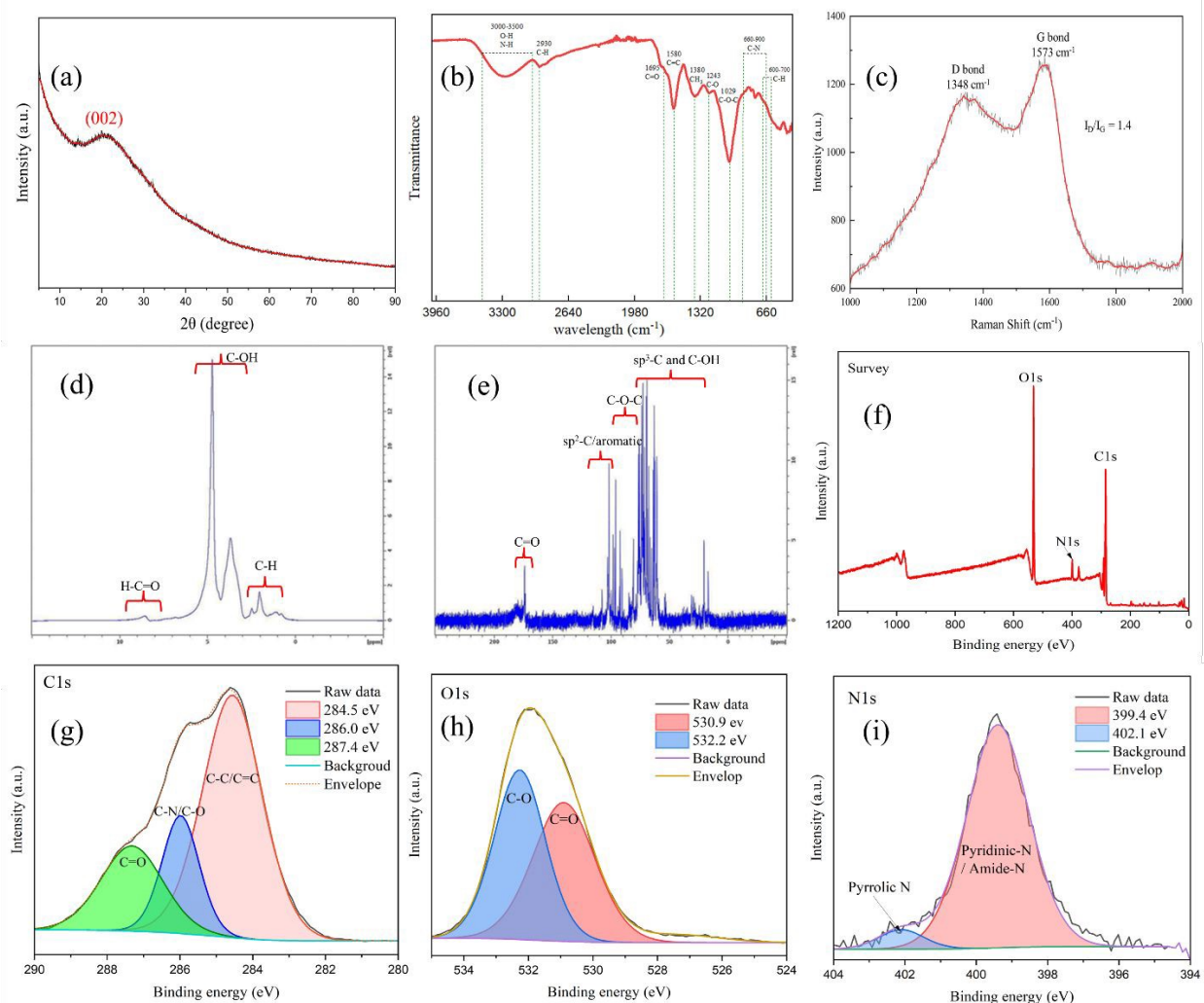


Figure 2 The structure analysis of the CQDs (*Sample 10*): (a) XRD patterns; (b) ATR-FTIR spectrum; (c) Raman spectrum; (d)  $^1\text{H}$  NMR spectrum; (e)  $^{13}\text{C}$  NMR spectrum; XPS spectrum survey scan (f) and corresponding expansion for (g) C1s, (h) O1s and (i) N1s peaks of the CQDs.

These results highlight the synergistic roles of  $\text{O}_2$  in photothermal and photocatalytic processes, leading to the formation of smaller, more uniform CQDs with enhanced fluorescence. The self-doping of nitrogen from corn stover contributed to a high quantum yield ( $20.1 \pm 0.8\%$ ), demonstrating an efficient and sustainable approach to CQD synthesis <sup>12</sup>.

To obtain high-purity CQDs, centrifugation and dialysis were employed to purify the sample (*Sample 10*) as described in *SI Appendix (Text S10)*. The purity of the CQDs was then evaluated using multiple analytical techniques, including LC-MS, ICP-MS, and IC to detect residual small molecules, metal ions, and anionic species (*SI Appendix, Text S11*). Figure 3 presents the comprehensive characterization of CQDs after purification by centrifugation and dialysis. HRTEM images (Figures 3a and 3f) reveal that the CQDs are uniformly dispersed, with average



diameters of  $3.1 \pm 1.4$  nm and  $3.7 \pm 1.6$  nm, respectively, confirming good size uniformity and monodispersity. The high-resolution image in Figure 3d shows clear lattice fringes with an interplanar spacing of 0.21 nm, corresponding to the (100) plane of graphitic carbon<sup>2</sup>, further supported by the FFT patterns in Figures 3b and 3e, indicating partial crystallinity. The 3D-EEM spectrum (Figure 3c) and accompanying photographs demonstrate strong fluorescence and excellent optical properties of the CQDs under UV light. AFM analysis (Figures 3g–i) further confirms the nanoscale size and uniform height distribution of individual CQDs, with a height range of ~3–4 nm and no visible aggregation. TEM analysis (*SI Appendix, Figure S12*) from multiple regions confirms the carbon quantum dots (CQDs) possess diameters ranging from approximately 3 to 4 nm, demonstrating that dialysis successfully yielded well-dispersed individual nanoparticles with no observable aggregation. These results confirm that centrifugation and dialysis effectively remove impurities while preserving the structural integrity, size uniformity, and fluorescence properties of the CQDs.



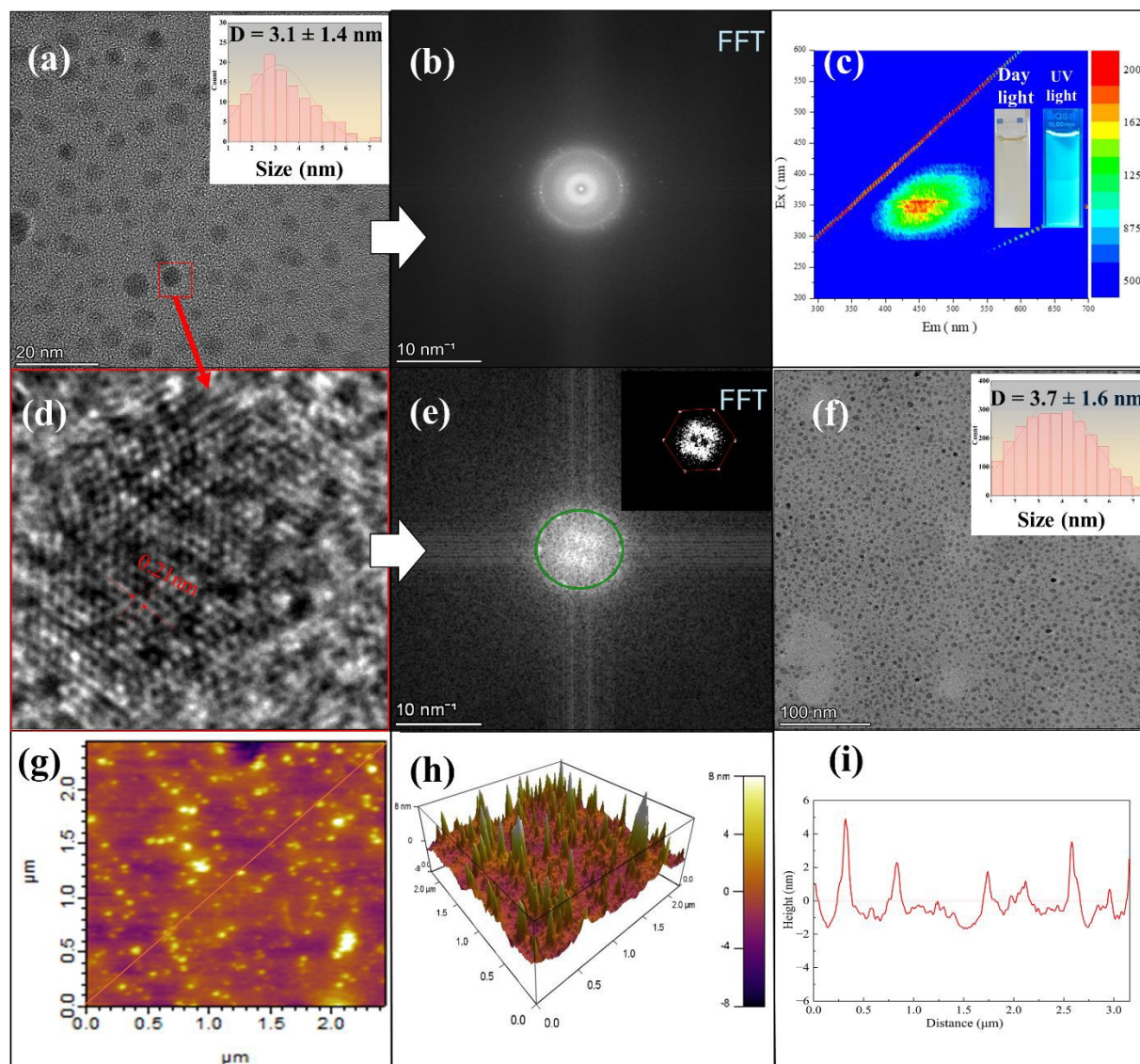


Figure 3. CQDs (*Sample 10*) after dialysis filtration: (a) HRTEM image and size distribution (scale bar: 20 nm); (b) Fast Fourier Transform (FFT) pattern corresponding to (a); (c) 3D-EEM fluorescence spectrum and the photograph of the CQDs solution under daylight and a handheld UV flashlight (Alonefire SV003, SVC 365 nm); (d) HRTEM image with lattice spacing indicated of the CQDs; (e) FFT pattern corresponding to (d); (f) HRTEM image and size distribution (scale bar: 100 nm); (g-i) AFM images of 2D, 3D, and the corresponding height-profile along the marked line in (g).

The key synthesis conditions, particle sizes, and quantum yields of representative samples are summarized in Table 1. To clarify how structural features govern photoluminescence (PL), we quantitatively compared particle size, surface chemistry, and graphitic domain structure across samples. TEM analysis (Figure 1 and Figure 2d) shows that CQDs synthesized under *light + rich-*



$O_2$  (*Sample 10*) are the smallest ( $4.6 \pm 0.8$  nm before purification;  $3.1 \pm 0.4$  nm after dialysis), whereas the oxygen-limited condition (*Sample 6*) produces much larger particles ( $29.8 \pm 13.5$  nm), and the dark-thermal condition (*Sample 8*) yields even larger amorphous structures ( $69.4 \pm 20.5$  nm). Correspondingly, *Sample 10* exhibits the strongest PL emission (*Figures S2–S5*), consistent with quantum confinement, while samples forming larger particles show weaker and broader emission. FTIR and XPS analyses (*Figure 2b*, *Figures 2f–i*) indicate that *Sample 10* contains abundant oxygen-containing functional groups (C=O, C–OH, epoxy), which are known to create radiative surface states that can enhance PL. Raman spectroscopy (*Figure 2c*) further shows an  $I_D/I_G$  ratio of 1.4 for *Sample 10*, indicating defect-rich  $sp^2$  nanodomains that are also associated with emissive sites. Together, these results demonstrate that bright PL arises from the combined effects of ultrasmall particle size, oxygen-rich surface states, and defect-engineered  $sp^2$  domains formed uniquely under simultaneous illumination and  $O_2$  supply.

Table 1. Summary of key synthesis conditions and representative properties of CQDs prepared under different reaction environments.

Sample	Key conditions	Particle size (nm)	Quantum yield (%)
<i>Sample 6</i>	Light: 834 mW cm <sup>-2</sup> ; atmosphere environment; 96 h;	$29.8 \pm 13.5$	13.7
<i>Sample 8</i>	Dark; heating to 50°C; atmosphere environment; 96 h;	$69.4 \pm 20.5$	9.0
<i>Sample 10</i>	Light: 834 mW cm <sup>-2</sup> ; rich- $O_2$ ; 96 h;	$4.6 \pm 0.8$ (after dialysis: $3.1 \pm 0.4$ )	$20.1 \pm 0.8$

### 3.3 Formation of CQDs from Corn Stover

The mechanism of CQDs formation from natural biomass remains incompletely established<sup>38</sup>. In this study, we propose a pathway involving photothermal and photocatalytic oxidation of lignin, hemicellulose, and cellulose in corn stover, primarily driven by the Fenton and Fenton-like reaction. This reaction employs *in situ*-generated  $H_2O_2$  (*SI Appendix, Figure S1e*) and naturally occurring metal ions (*SI Appendix, Table S3*). The system utilizes an ozone-free xenon lamp, ensuring that unwanted UV wavelengths (<260 nm) are filtered out to prevent ozone formation and associated side reactions.

#### 3.3.1 $H_2O_2$ Generation at Water Interfaces

Conventional  $H_2O_2$  production typically requires  $H_2O$ ,  $O_2$ , and photocatalysts under UV or solar irradiation<sup>39,40</sup>. In contrast, we demonstrate that interfacial water microenvironments formed by vaporization at the water-air interface can spontaneously and continuously generate  $H_2O_2$  under



simulated solar irradiation, without the need for additional catalysts. This phenomenon aligns with the interfacial charge-transfer mechanism reported previously <sup>24</sup>:



Another mechanism is electron transfer from  $\text{OH}^-$  to  $\text{H}^+$  at the interface, followed by  $\bullet\text{OH}$  radical recombination, while both  $\bullet\text{OH}$  and  $\bullet\text{H}$  have been detected experimentally using electron spin resonance spectroscopy (ESR) <sup>41</sup>. In addition, contact electrification at the water-solid interface <sup>42,43</sup> has been reported to contribute to  $\text{H}_2\text{O}_2$  formation.

In the present system, elevated solution temperatures ( $\sim 50$  °C) under illumination lead to partial water vaporization, followed by continuous condensation at the water-air interface, enabling continuous  $\text{H}_2\text{O}_2$  generation (Figure 4a).  $\text{H}_2\text{O}_2$  formation is further enhanced by UV radiation <sup>44</sup>, as confirmed using  $\text{H}_2\text{O}_2$  test strips (0–100 ppm) (*SI Appendix, Figure S1d*).

Building on the foundational discovery that  $\text{H}_2\text{O}$  at the hydrophilic-hydrophobic interface yields  $\text{H}_2\text{O}_2$  <sup>24,25</sup>, our approach further integrates simulated solar light to further enhance  $\text{H}_2\text{O}_2$  production through photochemical pathways. This strategy synergistically couples interfacial electrochemical processes with photochemical activation, enabling sustained  $\text{H}_2\text{O}_2$  generation without the need for external catalysts or energy-intensive UV sources, supporting a scalable and sustainable reaction pathway.

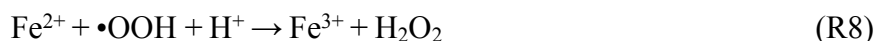
### 3.3.2 Acid Leaching of Metal Ions from Corn Stover

Protons ( $\text{H}^+$ ) and hydrogen atoms ( $\bullet\text{H}$ ) generated in this system facilitate the leaching of metal ions from corn stover into the aqueous phase. ICP-MS analysis (*SI Appendix, Table S3*) detected a concentration of 0.81 ppm ( $\text{Fe}^{2+}/\text{Fe}^{3+}$ ) in the CQD solution, confirming effective metal ion dissolution. The resulting Fenton reaction proceeds at a bulk solution pH of 5.02, although localized pH values near reactive interfaces may be lower during the reaction.

### 3.3.3 Fenton and Fenton-Like Reactions

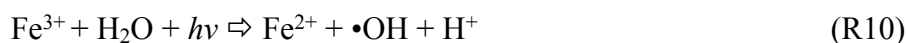
The classical Fenton process involves the following reactions <sup>45</sup>:





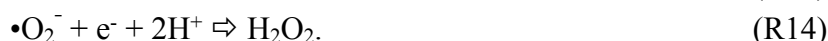
Hydroxyl radicals ( $\bullet\text{OH}$ ) generated through these reactions oxidatively degrade organic molecules in corn stover, facilitating CQD formation. In addition to iron, other multivalent metal ions (e.g., Co, Cr, Cu, Mn, Mo, Ru, Ti, W, and V) detected by ICP-MS (*SI Appendix, Table S3*) may participate in Fenton-like reactions, further contributing to reactive oxygen species generation<sup>46</sup>.

Simulated solar irradiation enhances the Fenton process through photo-induced reactions (Figure 4b)<sup>47</sup>, as described by the following equations:



These reactions continuously regenerate  $\text{Fe}^{2+}$  and produce additional  $\bullet\text{OH}$  radicals, accelerating oxidative degradation. Experimental results confirm that UV light (250–430 nm) plays a crucial role in CQD synthesis, as evidenced by increased fluorescence intensity and reduced pH, indicating enhanced formation of organic acids ( $-\text{COOH}$ ) during biomass degradation (*SI Appendix, Figure S5, Table S1*).

Molecular oxygen further promotes  $\text{Fe}^{3+}$  reduction and reactive oxygen species (ROS) generation<sup>48</sup>, as illustrated by the following reactions:



The resulting superoxide radicals ( $\bullet\text{O}_2^-$ ) reacts with  $\text{H}_2\text{O}$  to form additional  $\text{H}_2\text{O}_2$ , accelerating the photo-Fenton cycle<sup>49</sup>. An  $\text{O}_2$ -rich atmosphere consequently enhances the oxidative degradation of hemicellulose, cellulose, and lignin, boosting CQD yield (Figure 4c). In parallel, organic radical intermediates may undergo peroxo-organic transformations<sup>50,51</sup>, further amplifying oxidative pathways and promoting CQD formation.

ESR spin-trapping experiments was carried out to detect ROS formation and peroxide accumulation using DMPO (*SI Appendix, Figure S8*). *Figure S8a* exhibits a four-line ESR pattern of  $\text{H}_2\text{O}_2$  standards measured with  $\text{Fe}^{2+}$  triggering. In biomass-free controls (Figure S8b), illumination and  $\text{O}_2$  flow induce discernible ESR signals absent under dark conditions, indicating interfacial photochemical radical generation, although the spectra are broadened by overlapping ROS adducts. In the corn-stover-containing system (Figure S8c), ESR signals are weak and broadened due to the rapid radical consumption and heterogeneous scavenging by biomass-derived



organic species and redox-active sites. Notably,  $\text{Fe}^{2+}$  addition at extended reaction time (60 min) markedly enhances the ESR response, supporting the accumulation of peroxide species and their involvement in localized, transient radical activation during CQD formation.

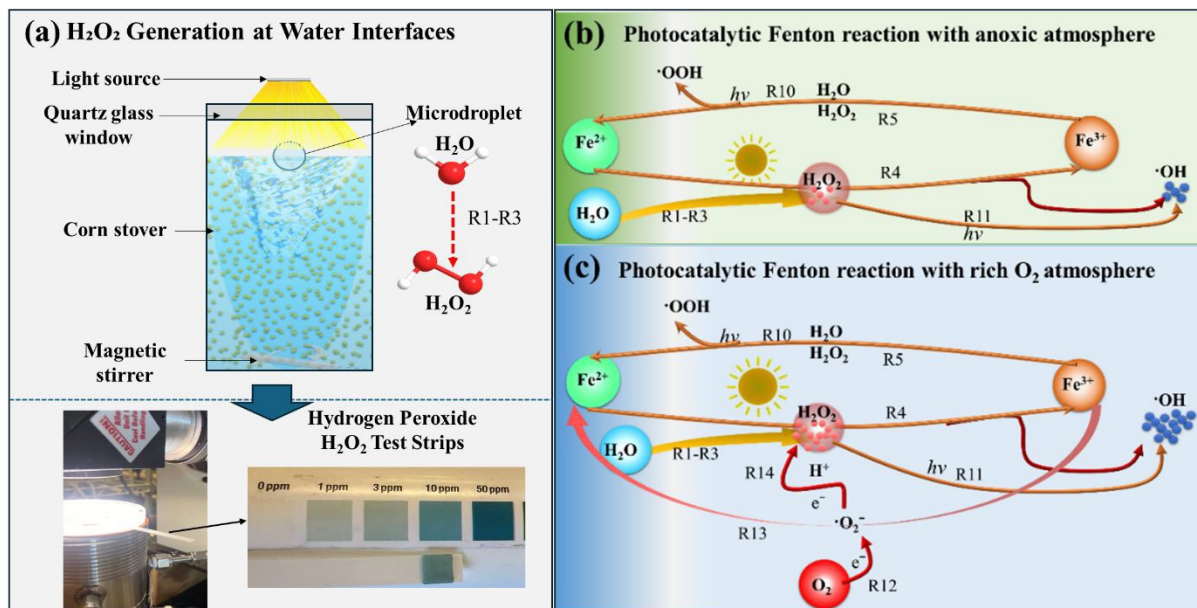


Figure 4 Proposed mechanism of peroxide generation and localized radical activation under illuminated conditions.

### 3.4 Corn Stover Conversion to CQDs

Corn stover primarily consists of cellulose (35-40%), hemicellulose (20-25%), lignin (19-22%) and trace metals (e.g.,  $\text{Fe}^{2+}$ )<sup>52</sup>. Control experiments using isolated cellulose, hemicellulose, and lignin as individual precursors yielded markedly weaker fluorescence under identical reaction conditions (*SI Appendix, Figure S6*), displaying the hemicellulose and lignin are easier to be degraded and contributed to the CQD production.

Hemicellulose, a heteropolymer of sugars (xylan, glucan), and lignin, a complex phenylpropanoid network, undergo preferential oxidative degradation in this system, while the proposed pathway of CQD production is shown in Figure 5. Hydroxyl radicals ( $\cdot\text{OH}$ ) cleave glycosidic (C–O–C) linkages in polysaccharides and  $\beta$ -O-4 ether bonds, fragmenting these macromolecules into monomeric and oligomeric sugars as well as phenolic compounds (e.g., vanillin, syringol, guaiacol)<sup>53,54</sup>. Notably, as-formed CQDs may enhance Fenton reactions by acting as photocatalysts, promoting  $\cdot\text{OH}$  radical production<sup>55–57</sup>. Their surface carboxyl functional groups can lower the solution pH, thereby optimizing reaction efficiency<sup>54</sup>. Consistent with this interpretation, the solution pH decreased with prolonged reaction time and higher  $\text{O}_2$  flow rates,



reaching 4.09 under O<sub>2</sub>-rich conditions (*SI Appendix, Table S1, Sample 10*), indicating enhanced organic acid formation and controlled H<sub>2</sub>O<sub>2</sub> consumption.

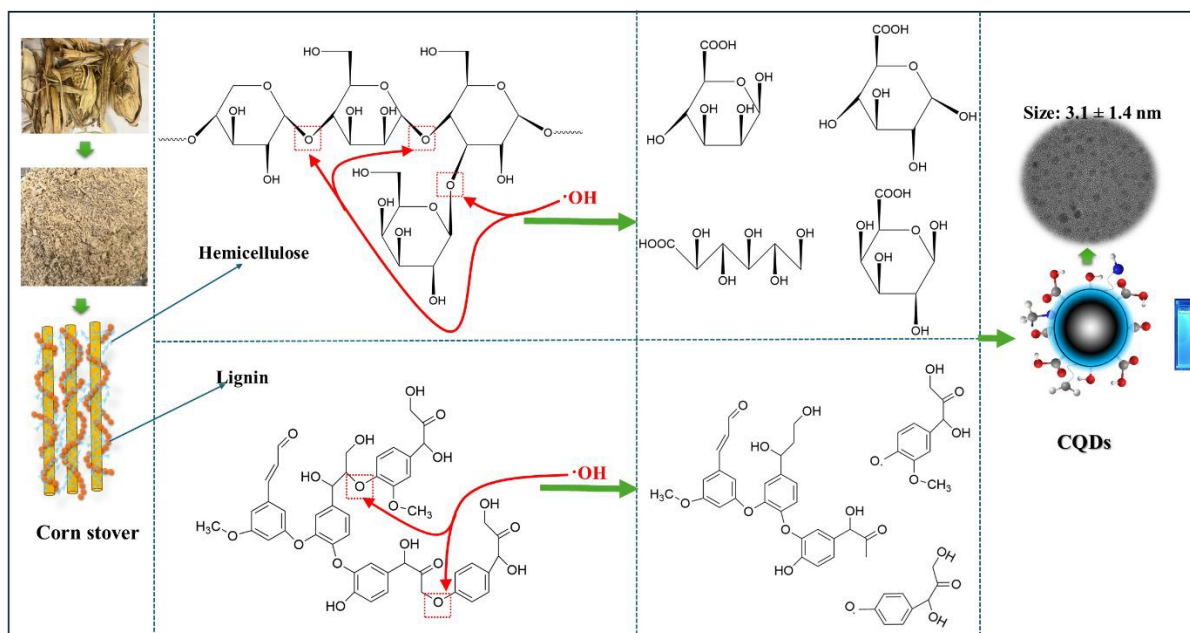


Figure 5 Proposed pathway for CQD formation from corn stover via peroxide-mediated oxidative depolymerization.

### 3.5 Comparison with Conventional CQD Synthesis Methods

For comparison, Tables S6–S8 systematically evaluate reported CQD synthesis methods in terms of raw materials, reaction conditions, CQD sizes, quantum yields, and environmental considerations.

Table S6 compares CQD synthesis routes involving high-temperature pyrolysis ( $\geq 300^\circ\text{C}$ ), two-step carbonization, or hydrothermal methods with added chemicals. These methods often require elevated temperatures ( $300 - 700^\circ\text{C}$ ) or strong acids, bases, or oxidants, which can complicate purification and introduce secondary environmental burdens, despite achieving high quantum yields in some cases. Table S7 focuses on one-step hydrothermal and photothermal CQD synthesis using only biomass and water. Compared with hydrothermal processes reported by other groups, the present photothermal method operates at substantially lower temperatures, requires less stringent equipment, and produces fewer liquid organic byproducts, resulting in easier CQD separation and higher product purity. Although several hydrothermal studies report higher quantum yields, these typically rely on higher temperatures or fresh biomass sources rich in soluble carbon, which are more readily degraded than solid lignocellulosic feedstocks. Table S8 compares CQD synthesis strategies based on externally added H<sub>2</sub>O<sub>2</sub> and catalysts with those relying on



internally generated  $\text{H}_2\text{O}_2$ . In contrast to methods requiring large  $\text{H}_2\text{O}_2$  dosages and added catalysts (e.g.,  $\text{Fe}^{2+}/\text{Fe}^{3+}$  or  $\text{W}_{18}\text{O}_{49}$ ), the present approach generates  $\text{H}_2\text{O}_2$  in situ without external oxidants or catalysts. This eliminates the need for costly reagents, reduces overoxidation of carbon precursors, enables smaller CQD sizes, and lowers overall energy demand due to the mild reaction temperature.

Overall, this work demonstrates a green and economically attractive CQD synthesis route that combines renewable biomass, internally generated oxidants, ambient-pressure operation, and low thermal input, offering clear advantages over conventional high-temperature or chemically intensive methods.

#### 4. Conclusions

This CQD synthesis strategy minimizes byproducts, simplifies purification, and eliminates harsh acids (e.g.,  $\text{H}_2\text{SO}_4$ ,  $\text{HNO}_3$ ). By leveraging corn stover as both a carbon source and a natural catalytic reservoir, it efficiently integrates spontaneous  $\text{H}_2\text{O}$ -to- $\text{H}_2\text{O}_2$  conversion under solar irradiation, providing an environmentally sustainable route for high-purity CQD production. These results extend microdroplet chemistry into the realm of biomass valorization and highlight a sustainable, external-catalyst-free strategy for converting raw biomass into high-quality nanocarbon materials.

#### Author contributions

M. Fan, X. Kang, and R.N. Zare designed research concepts; X. Kang performed the major research tasks, including tests and data analyses, and prepared the initial draft of the manuscript. Q. Yang, S. X. Tang, Z. Chen, S. Budhathoki, R. Paneru, S. Kim and A. Goroncy assist X. Kang in performing the research tasks. Y. Bai, Qian Li, and Z. Chen assisted M. Fan, X. Kang, and R. N. Zare in developing the research concepts. X. Kang, M. Fan, and R.N. Zare worked together to finalize the manuscript.

#### Conflict of Interest

The authors declare no conflict of interest.

#### Data availability

All data supporting the findings of this study are available within the paper and its Supporting Information. The Supporting Information (*Text S1–S11*, *Figures S1–S12*, and *Tables S1–S8*) provides additional experimental details and analyses, including the effects of light intensity, reaction time, oxygen flow, light wavelength ranges, and separated corn stover components, as



well as descriptions of Fenton and Fenton-like reactions, thermogravimetric analysis, ESR spectra, and purification protocols with purity evaluation. Characterization data (TEM, 3D-EEM, TGA, LC-MS, ICP-MS, IC, and pH) together with tables containing comparisons to conventional CQD synthesis methods as well as their reported quantum yields of CQDs are also provided.

## Acknowledgment

We would like to thank Zhaojie Zhang for the help with fluorescence microscope measurements. This work was supported by the University of Wyoming and Czech University of Life Sciences Prague.

## References

- 1 S. Y. Lim, W. Shen and Z. Gao, *Chem Soc Rev*, 2015, 44, 362–381.
- 2 W. Li, W. Zhou, Z. Zhou, H. Zhang, X. Zhang, J. Zhuang, Y. Liu, B. Lei and C. Hu, *Angewandte Chemie - International Edition*, 2019, 131, 7356–7361.
- 3 L. Wang, W. Li, L. Yin, Y. Liu, H. Guo, J. Lai, Y. Han, G. Li, M. Li, J. Zhang, R. Vajtai, P. M. Ajayan and M. Wu, *Sci Adv*, 2020, 6, eabb6772.
- 4 Y. Li, X. Zhang, W. Hou, Z. Zhou, S. Zhang, H. Guo, J. Zhang, J. Xu and L. Wang, *Appl Catal B*, 2026, 380, 125758.
- 5 X. Xu, R. Ray, Y. Gu, H. J. Ploehn, L. Gearheart, K. Raker and W. A. Scrivens, *J Am Chem Soc*, 2004, 126, 12736–12737.
- 6 R. Liu, D. Wu, S. Liu, K. Koynov, W. Knoll and Q. Li, *Angewandte Chemie - International Edition*, 2009, 48, 4598–4601.
- 7 L. Cao, X. Wang, M. J. Meziani, F. Lu, H. Wang, P. G. Luo, Y. Lin, B. A. Harruff, L. M. Veca, D. Murray, S. Y. Xie and Y. P. Sun, *J Am Chem Soc*, 2007, 129, 11318–11319.
- 8 A. Xu, G. Wang, Y. Li, H. Dong, S. Yang, P. He and G. Ding, *Small*, 2020, 16, 2004621.
- 9 S. Chen, S. Z. Zhang and H. Jiang, *ACS ES and T Water*, 2024, 4, 531–542.
- 10 S. N. Baker and G. A. Baker, *Angewandte Chemie - International Edition*, 2010, 49, 6726–6744.
- 11 S. Chung, R. A. Revia and M. Zhang, *Advanced Materials*, 2021, 33, 1904362.
- 12 R. Paneru, X. Kang, S. Budhathoki, Z. Chen, Q. Yang, S. T. Tjeng, Q. Dai, W. Wang, J. Tang and M. Fan, *Journal of Environmental Sciences*, 2025, 154, 590–601.



- 13 H. Ding, S. B. Yu, J. S. Wei and H. M. Xiong, *ACS Nano*, 2016, 10, 484–491.
- 14 B. Dutcher, M. Fan, B. Leonard, M. D. Dyar, J. Tang, E. A. Speicher, P. Liu and Y. Zhang, *Journal of Physical Chemistry C*, 2011, 115, 15532–15544.
- 15 M. Yang, L. Guo, G. Hu, X. Hu, J. Chen, S. Shen, W. Dai and M. Fan, *Ind Eng Chem Res*, 2016, 55, 757–765.
- 16 P. M. Gawal and A. K. Golder, *Colloids Surf A Physicochem Eng Asp*, 2024, 683, 133068.
- 17 T. J. Pillar-Little, N. Wanninayake, L. Nease, D. K. Heidary, E. C. Glazer and D. Y. Kim, *Carbon N Y*, 2018, 140, 616–623.
- 18 D. Xu, C. Yu, X. Peng, H. Yan and Y. Zhang, *Research on Chemical Intermediates*, 2024, 50, 4597–4617.
- 19 V. G. Matveeva and L. M. Bronstein, *Prog Mater Sci*, 2022, 130, 100999.
- 20 S. C. Perry, D. Pangotra, L. Vieira, L. I. Csepei, V. Sieber, L. Wang, C. Ponce de León and F. C. Walsh, *Nat Rev Chem*, 2019, 3, 442–458.
- 21 X. Zhou, Y. Zhang, C. Wang, X. Wu, Y. Yang, B. Zheng, H. Wu, S. Guo and J. Zhang, *ACS Nano*, 2012, 6, 6592–6599.
- 22 C. Zhu, S. Yang, G. Wang, R. Mo, P. He, J. Sun, Z. Di, Z. Kang, N. Yuan, J. Ding, G. Ding and X. Xie, *J Mater Chem B*, 2015, 3, 6871–6876.
- 23 D. Y. Lee, Z. Haider, S. K. Krishnan, T. Kanagaraj, S. H. Son, J. Jae, J. R. Kim, P. S. Murphin Kumar and H. il Kim, *Chemosphere*, 2024, 361, 142330.
- 24 M. A. Mehrgardi, M. Mofidfar and R. N. Zare, *J Am Chem Soc*, 2022, 144, 7606–7609.
- 25 J. K. Lee, K. L. Walker, H. S. Han, J. Kang, F. B. Prinz, R. M. Waymouth, H. G. Nam and R. N. Zare, *Proc Natl Acad Sci U S A*, 2019, 116, 19294–19298.
- 26 J. K. Lee, H. S. Han, S. Chaikasettin, D. P. Marron, R. M. Waymouth, F. B. Prinz and R. N. Zare, *Proc Natl Acad Sci U S A*, 2020, 117, 30934–30941.
- 27 X. Song, C. Basheer, J. Xu and R. N. Zare, *Sci. Adv*, 2024, 10, 4443.
- 28 Y. Meng, Y. Xia, J. Xu and R. N. Zare, *Sci. Adv*, 2025, 11, 8979.
- 29 H. Kalita, J. Mohapatra, L. Pradhan, A. Mitra, D. Bahadur and M. Aslam, *RSC Adv*, 2016, 6, 23518–23524.



- 30 A. Afzalalghom, A. Beitollahi, S. M. Mirkazemi, M. Maleki and H. Sarpoolaky, *Small*, 2024, 20, 2308082.
- 31 B. Al-Hashimi, K. M. Omer and H. S. Rahman, *Arabian Journal of Chemistry*, 2020, 13, 5151–5159.
- 32 N. B. Mandava, in *Handbook of Natural Pesticides: Methods*, CRC Press, 2019, pp. 219–256.
- 33 H. Nie, M. Li, Q. Li, S. Liang, Y. Tan, L. Sheng, W. Shi and S. X. A. Zhang, *Chemistry of Materials*, 2014, 26, 3104–3112.
- 34 S. Moonrinta, B. Kwon, I. In, S. Kladsomboon, W. Sajomsang and P. Paoprasert, *Opt Mater (Amst)*, 2018, 81, 93–101.
- 35 A. C. Ferrari and D. M. Basko, *Nat Nanotechnol*, 2013, 8, 235–246.
- 36 S. Zhu, Q. Meng, L. Wang, J. Zhang, Y. Song, H. Jin, K. Zhang, H. Sun, H. Wang and B. Yang, *Angewandte Chemie - International Edition*, 2013, 52, 4045–4049.
- 37 B. De and N. Karak, *RSC Adv*, 2013, 3, 8286–8290.
- 38 M. Si, J. Zhang, Y. He, Z. Yang, X. Yan, M. Liu, S. Zhuo, S. Wang, X. Min, C. Gao, L. Chai and Y. Shi, *Green Chemistry*, 2018, 20, 3414–3419.
- 39 C. Pan, G. Bian, Y. Zhang, Y. Lou, Y. Zhang, Y. Dong, J. Xu and Y. Zhu, *Appl Catal B*, 2022, 316, 121675.
- 40 T. Liu, Z. Pan, J. J. M. Vequizo, K. Kato, B. Wu, A. Yamakata, K. Katayama, B. Chen, C. Chu and K. Domen, *Nat Commun*, 2022, 13, 1034.
- 41 J. Li, Y. Xia, X. Song, B. Chen and R. N. Zare, *Proc Natl Acad Sci U S A*, 2024, 121, e2318408121.
- 42 A. Gallo Jr., N. H. Musskopf, X. Liu, Z. Yang, J. Petry, P. Zhang, S. Thoroddsen, H. Im and H. Mishra, *Chem Sci*, 2022, 13, 2574–2583.
- 43 B. Chen, Y. Xia, R. He, H. Sang, W. Zhang, J. Li, L. Chen, P. Wang, S. Guo, Y. Yin, L. Hu, M. Song, Y. Liang, Y. Wang, G. Jiang and R. N. Zare, *Proc Natl Acad Sci U S A*, 2022, 119, e2209056119.
- 44 B. C. Faust, C. Anastasio, J. M. Allen and T. Arakaki, *Science (1979)*, 1993, 260, 73–75.
- 45 J. De Laat and H. Gallard, *Environ Sci Technol*, 1999, 33, 2726–2732.



- 46 Y. Liu and J. Wang, *Chemical Engineering Journal*, 2023, 466, 143147.
- 47 J. Kiwi, C. Pulgarin and P. Peringer, *Appl Catal B*, 1994, 3, 143147.
- 48 S. Chen, Y. Chen, Y. Zhang, X. Kuang, Y. Liu, M. Guo, L. Ma, D. Zhang and Q. Li, *Front Neurosci*, 2020, 14, 601193.
- 49 P. Zhou, J. Xu, J. Guo, X. Hou, L. Dai, X. Xiao and K. Huo, *Green Chemistry*, 2024, 26, 6005–6018.
- 50 O. Legrini, E. Oliveros and A. M. Braun, *Chem Rev*, 1993, 93, 671–698.
- 51 B. Utset, J. Garcia, J. Casado, X. Domènech and J. Peral, *Chemosphere*, 2000, 41, 1187–1192.
- 52 A. H. Rony, L. Kong, W. Lu, M. Dejam, H. Adidharma, K. A. M. Gasem, Y. Zheng, U. Norton and M. Fan, *Bioresour Technol*, 2019, 284, 466–473.
- 53 D. Van Eylen, F. van Dongen, M. Kabel and J. de Bont, *Bioresour Technol*, 2011, 102, 5995–6004.
- 54 E. Mnich, N. Bjarnholt, A. Eudes, J. Harholt, C. Holland, B. Jørgensen, F. H. Larsen, M. Liu, R. Manat, A. S. Meyer, J. D. Mikkelsen, M. S. Motawia, J. Muschiol, B. L. Møller, S. R. Møller, A. Perzon, B. L. Petersen, J. L. Ravn and P. Ulvskov, *Nat Prod Rep*, 2020, 37, 919–961.
- 55 T. Zhang, Y. Wen, Z. Pan, Y. Kuwahara, K. Mori, H. Yamashita, Y. Zhao and X. Qian, *Environ Sci Technol*, 2022, 56, 2617–2625.
- 56 Y. Yang, Q. Guo, Q. Li, L. Guo, H. Chu, L. Liao, X. Wang, Z. Li and W. Zhou, *Adv Funct Mater*, 2024, 34, 2400612.
- 57 W. Han, H. Zhang, D. Li, W. Qin, X. Zhang, S. Wang and X. Duan, *Appl Catal B*, 2024, 350, 123918.



## Data Availability Statement

All data supporting the findings of this study are available within the paper and its Supporting Information. The Supporting Information (*Text S1–S11, Figures S1–S12, and Tables S1–S8*) provides additional experimental details and analyses, including the effects of light intensity, reaction time, oxygen flow, light wavelength ranges, and separated corn stover components, as well as descriptions of Fenton and Fenton-like reactions, thermogravimetric analysis, ESR spectra, and purification protocols with purity evaluation. Characterization data (TEM, 3D-EEM, TGA, LC-MS, ICP-MS, IC, and pH) together with tables containing comparisons to conventional CQD synthesis methods as well as their reported quantum yields of CQDs are also provided.

